Journal of
Synchrotron Radiation

ISSN 0909-0495

Received 15 June 2004
Accepted 4 November 2004

Phase-contrast X-ray imaging combining free space propagation and Bragg diffraction

Paola Coan,* Elodie Pagot, Stefan Fiedler, Peter Cloetens, José Baruchel and Alberto Bravin

European Synchrotron Radiation Facility, 6 Rue Jules Horowitz, BP 220, 38043 Grenoble CEDEX, France. E-mail: coan@esrf.fr

The combination of X-ray 'propagation-based' and 'analyzer-based' phase-contrast imaging with a perfect crystal-analyzer is investigated. The image pattern produced using this 'hybrid' imaging technique presents peculiar features that can be interpreted as a mixture of the two independent phase-contrast signals. A quantitative analysis has been performed in terms of signal-to-noise ratio for the three techniques considered in this paper. Results show that in the 'hybrid imaging' technique this parameter has a weaker dependence on the angular alignment of the crystal analyser with respect to the 'analyser-based' imaging. This pioneering experiment indicates that this hybrid imaging technique might permit simultaneous advantage of the specific features of the two imaging methods to be taken.

Keywords: phase contrast; X-ray imaging; Fresnel diffraction; analyzers; X-ray source coherence.

1. Introduction

Radiography based on absorption is a standard tool for imaging objects with hard X-rays. For studies on weakly absorbing materials the attenuation in the sample often becomes too small to give detectable contrast. An alternative approach is offered by the phase-contrast imaging techniques, which can provide improved image contrast (Fitzgerald, 2000).

These techniques are sensitive to phase shifts of an electromagnetic wave passing through an object; such shifts originate by variations of the optical path whose values are determined by d, the decrement with respect to unity of the refraction coefficient, which is related to the real part of the susceptibility of the scattering material $\delta = -\chi_{0r}/2$. Despite their common origin, phase-contrast imaging techniques have been theoretically and experimentally treated separately in the literature.

In this work we show that, by using a coherent X-ray beam and choosing an appropriate set-up that combines propagation as well as diffraction by a crystal analyzer, the resulting images will show original features. This technique is introduced in this paper as 'hybrid phase-contrast imaging' (HI).

2. Phase-sensitive techniques

In order to exploit the phase effects for imaging, different techniques have been developed. They include propagation-based imaging (PB) (Snigirev *et al.*, 1995; Cloetens *et al.*, 1996; Nugent *et al.*, 1996), analyzer-based imaging (AB) (Förster *et al.*, 1980; Somenkov *et al.*, 1991; Davis *et al.*, 1995; Chapman *et al.*, 1997; Bravin, 2003) and interferometric techniques (Momose *et al.*, 1996; David *et al.*, 2002). Coherent imaging modalities have significant application in various fields such as material science (Tsai *et al.*, 2002; Cloetens *et al.*, 2002), submicrometer imaging (Lagomarsino *et al.*, 1997; Hignette *et al.*, 2003) and biomedical imaging (Arfelli *et al.*, 2000).

The PB technique does not require any supplementary optics and consists in recording the interference pattern produced by choosing one or several sample-to-detector distances. The framework for the theoretical description of the technique is Fresnel diffraction (Born & Wolf, 1999).

The AB technique consists in placing a perfect crystal in Bragg or Laue (Ingal & Beliaevskaya, 1995) geometry between the sample and the detector. The crystal acts as a filter for the radiation refracted and scattered inside the object, since it only accepts a narrow range of angles of the incident beam centered at the Bragg angle for the specific energy. Before being detected, the beam is modulated by the reflectivity curve of the crystal.

To be able to perform phase-contrast imaging, the X-ray beam has to fulfil conditions concerning the temporal (longitudinal) and spatial (transverse) coherence properties of the radiation that are respectively linked to the X-ray monochromaticity and to the angular source size.

The temporal coherence condition ($\Delta\lambda/\lambda \ll 1$) is usually a strong requirement in the case of the analyzer-based imaging technique, but it is easily satisfied in synchrotron radiation facilities using perfect crystal monochromators ($\Delta\lambda/\lambda \simeq$

10^{-4}). In the case of propagation, even a polychromatic spectrum generated by a conventional microfocus X-ray tube can be used (Wilkins *et al.*, 1996; Pogany *et al.*, 1997).

On the contrary, the need of spatial coherence is more stringent for propagation-based phase-contrast imaging. The degree of coherence that indicates the correlation of the amplitudes of waves between different points transverse to the direction of propagation is usually expressed in terms of lateral (or transverse) coherence length $l_c = \lambda/2\alpha$, where $\alpha = S/L$; L and S are the source–object distance and the dimension of the source, respectively.

If the detail set on the object plane has dimensions smaller (or of the same order) than l_c, it will see the X-ray beam as coherent and it could produce observable phase effects by an appropriate choice of the sample-to-detector distance (z) and of the spatial resolution of the detector. In fact, in the case of small angular source sizes, z can be varied at will in the meter range without appreciable blurring of the image ($z \cdot \alpha$).

Concerning the AB technique, the requirement is that α, as seen by the sample, is smaller than the Darwin width of the crystal analyzer. If the initial beam already satisfies this condition, there is no loss of intensity by the monochromatization/collimation process upstream of the sample.

For long synchrotron radiation beamlines such as ID19 at the ESRF (~145 m), the transverse coherence length can be as high as 140 µm at 25 keV in the vertical direction; in the case of a microfocus tube with a typical source size of 20 µm, $l_c = 0.6$ µm for $z = 0.5$ m.

3. Materials and methods

The experiment was performed at the ID19 beamline of the European Synchrotron Radiation Facility (ESRF, Grenoble, France). The X-ray source used was an 11-pole variable-field wiggler ($B_{max} = 1.4$ T), which delivers a spectrally and spatially homogeneous X-ray beam with tunable photon energy between 6 and 100 keV. The long source-to-sample distance (~145 m), in combination with the very small dimensions of the source [25 µm (V) × 125 µm (H), expressed as full width at half-maximum (FWHM)], leads to a highly coherent X-ray beam. A fixed-exit double-crystal silicon (111) monochromator operating in reflection geometry in the vertical plane provides an X-ray beam of up to 14 mm (V) × 40 mm (H) at the sample position. Images have been recorded with a FRELON CCD-based X-ray detector system with an effective pixel size of 7.5 µm × 7.5 µm, producing images with a spatial resolution of about 16 µm (Cloetens, 1999).

Fig. 1 shows schematically the different experimental configurations used in this paper: (*a*) set-up used for PB images, the sample-to-detector distance varying from 0 to 7 m, (*b*) set-up for AB, where the X-ray beam analyzer is a Si(111) crystal operating in Bragg geometry with a vertical diffraction plane, (*c*) set-up for the HI technique in which the wave transmitted by the sample is analyzed by the Si(111) crystal after propagation in the air. The experimental data have been acquired using 25 keV X-rays; the measured analyzer rocking-curve width (FWHM) is 14.5 µrad.

Table 1
Some physical parameters of the two samples used for this study.

In the last column, the calculated maximum absorption contrast is reported.

Sample	Diameter (µm)	Material	Density (g cm^{-3})	δ	Contrast
Wire 1	350	Nylon	0.93	3.52×10^{-7}	1%
Wire 2	100	Kevlar	1.44	5.45×10^{-7}	0.5%

The AB and HI images have been recorded at different angular positions (intervals of 2.8 µrad) along the rocking curve that is centered at the Bragg angle for the Si (111) reflection at 25 keV ($\Delta\theta = 0$). Every image has been normalized by acquiring a supplementary image after having removed the sample from the X-ray beam.

In order to visualize only the phase effects, thin cylindrical polymer fibers have been chosen as the sample because they can be considered as pure phase objects, showing almost negligible absorption contrast at this photon energy. The sample characteristics are summarized in Table 1.

4. Data analysis and discussion

Fig. 2 shows the images and the extracted intensity profiles acquired using the PB, AB and HI techniques. In the case of the AB technique, each edge of the object gives rise to a peak that can be either positive or negative. The signal is evaluated by calculating the difference between the recorded peak and

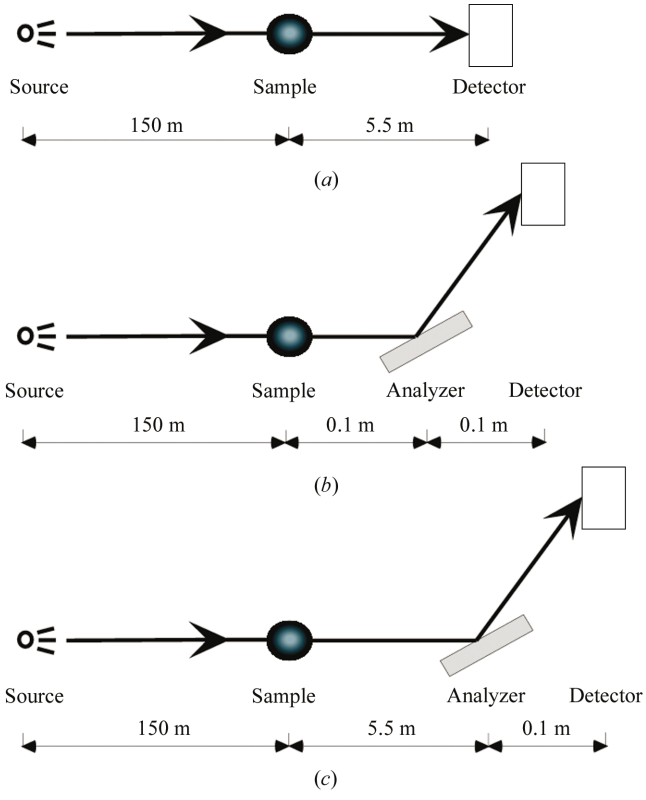

Figure 1
Schematic representation of the set-ups used for the image acquisition in the PB (*a*), AB (*b*) and HI (*c*) configurations.

the background. Both edges of the wire in the PB images show symmetrical contrast, with contiguous positive and negative peaks. This occurs also in the HI images, owing to the combination of the propagation and analyzer effects. In these cases, the signal is calculated as the difference between each maximum and minimum signal.

The quantitative analysis has been carried out by evaluating the signal-to-noise ratio (SNR). The SNR has been calculated using the relation $\mathrm{SNR} = A^{1/2}(I_{\max} - I_{\min})/I_0\sigma_0$, where A is the area (in pixels) over which the signal has been evaluated as the mean of the pixel counts (Evans, 1981); I_0 is the average of several values of the background intensity, each one being the mean of the pixel counts over a different area A on the background, and σ_0 is the related standard deviation; $I_{\max}$ and $I_{\min}$ represent the maximum and the minimum of the diffraction pattern produced by an edge with respect to the background. In particular, in the case of a single positive or negative peak, $I_{\min}$ and $I_{\max}$ correspond to the background values, respectively. The shown SNR values (Fig. 5) have been obtained by averaging repeated evaluations of this parameter on the recorded images and the reported error bars are the calculated standard deviations.

Fig. 3 shows the experimental profiles for the nylon wire using the three imaging techniques. The PB image has been acquired at 5.5 m from the sample and the AB and HI profiles are shown at four different positions on the rocking curve. The PB signal contrast, evaluated as $(I_{\mathrm{signal}} - I_0)/I_0$, is as high as 27%; the AB signal increases from a minimum of 3% at $\Delta\theta = 0$ to a maximum of 55% at $\Delta\theta$ = 11.2 µrad, while at the same angular positions the HI shows values of 26% and 46%, respectively.

In the PB images the signal is determined in first approximation by the Laplacian of the phase introduced by the object and by the sample–detector distance, while in the AB images the wave passes through the crystal acting like a bandpass filter; thus only some frequencies can reach the detector. The HI signal combines the propagation and diffraction effects, and it has been compared with the sum of the PB and AB signals in Fig. 4. As expected, the calculated profile fits only approximately with the experimental HI signal, indicating that the latter is also an interference phenomenon (Pavlov *et al.*, 2004).

Fig. 5 shows the graph of the SNR *versus* the angular setting of the analyzer, for the two edges of the wires imaged with the AB and the HI techniques. The SNR values for the left and right edge in the PB configuration are, respectively, 178.5 ± 29.8 and 164.5 ± 12.3 for the nylon wire and 241.9 ± 29.9 and 207.2 ± 24.9 for the kevlar wire. The visibility of the two edges, expressed in terms of SNR, changes substantially by varying the angle of the crystal. The profiles for the left and the

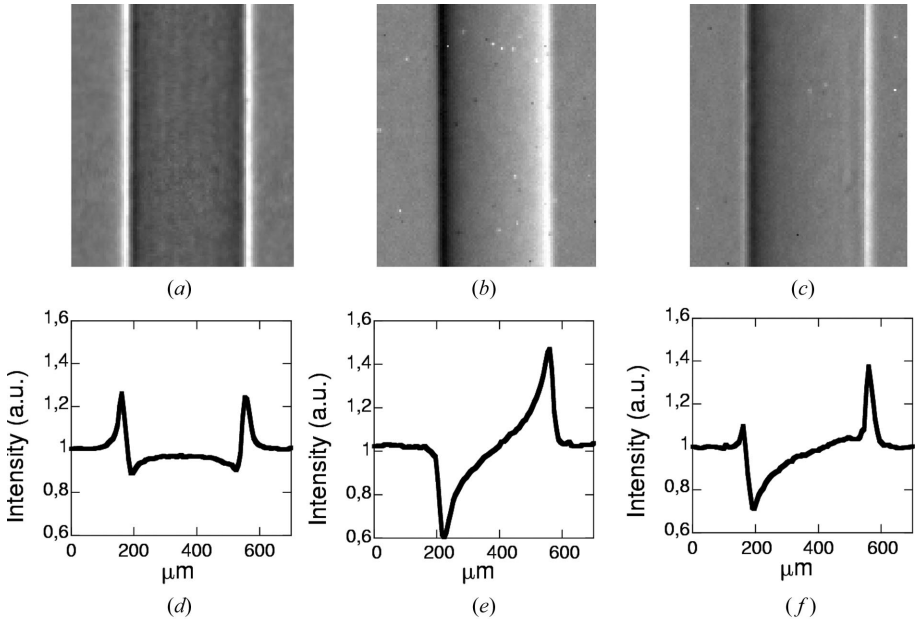

Figure 2
Images and vertical profiles of the nylon wire with the PB (*a*, *d*), the AB (*b*, *e*) and HI (*c*, *f*) techniques.

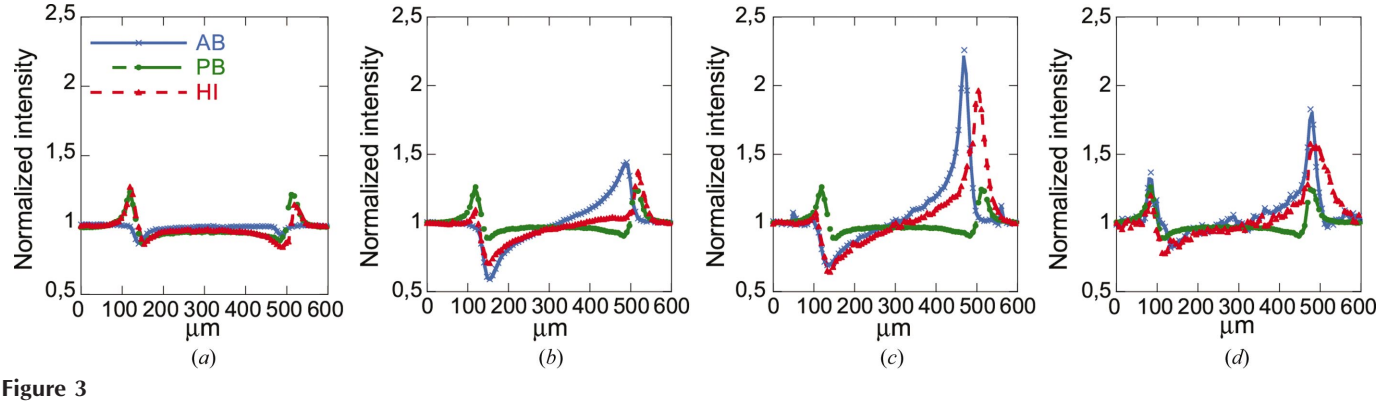

Figure 3
Signal profiles (evaluated by averaging the signal over 30 pixels) of the nylon wire at four different angular positions along one flank of the rocking curve of the analyzer: $\Delta\theta = 0$ (*a*), $\Delta\theta = 5.6$ µrad (*b*), $\Delta\theta = 11.2$ µrad (*c*) and $\Delta\theta = 16.8$ µrad (*d*). The PB profile, related to a sample-to-detector distance of 5.5 m, appears in each plot for comparison with the signals obtained in the AB and HI configurations.

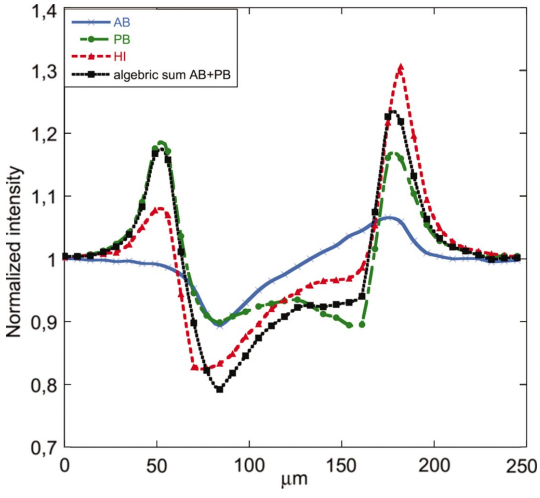

Figure 4
PB, AB and HI signal profiles of the kevlar wire compared with the calculated profile obtained by algebraically summing the PB and AB signals at $\Delta\theta = 2.8$ μrad.

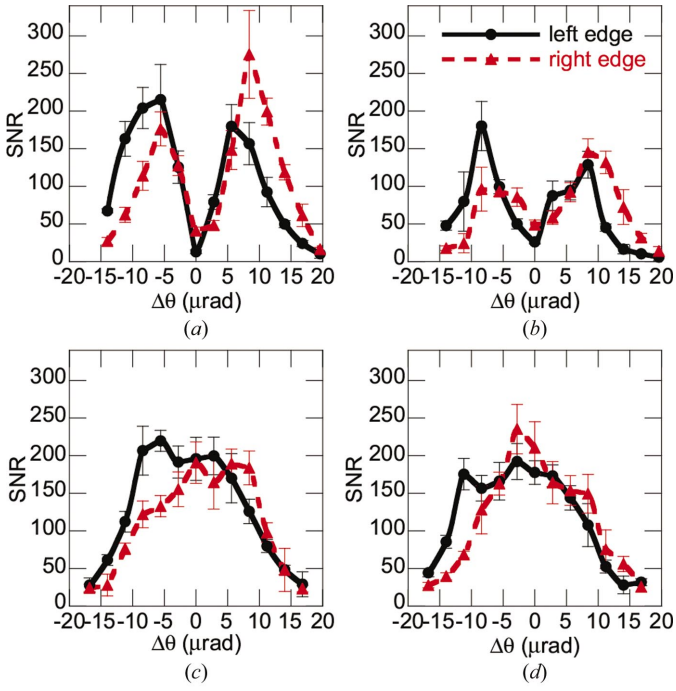

Figure 5
Signal-to-noise ratio values of the signal produced by the edges of the two wires as a function of the angular position along the rocking curve of the analyzer for the AB [nylon wire (*a*), kevlar wire (*b*)] and HI [nylon wire (*c*), kevlar wire (*d*)] configurations.

right edge are approximately mirrors of each other with respect to the center of the curve ($\Delta\theta = 0$). The slight difference in the absolute values can be explained by imperfections in the sample shape.

In AB, this behaviour can be explained by considering the different origin of the signal for the various angular positions. In particular, while at $\Delta\theta = 0$ the signal mainly derives from refraction and the reduction of the scattering component on the image (and, in thicker samples, from X-ray absorption), for the other angular positions the signal is determined by the alignment of the analyzer with respect to a given direction of the refracted X-rays. Therefore, by rocking the crystal, it is possible to optimize the visibility of the details that, in the case of the studied wires, presents maximum values of the SNR for positions on the shoulders of the rocking curve. In other words, at around $\Delta\theta = 0$ there is a minimum of the derivative of the rocking curve, and then the crystal is less sensitive to X-rays refracted inside the object, determining a low SNR. On the tails of the rocking curve, the low reflectivity increases the noise on images, also reducing the SNR.

In the case of the HI technique, the main difference with respect to AB concerns the SNR values around the exact Bragg angle. In fact, while the AB signal is maximum on the shoulders of the rocking curve and it decreases towards $\Delta\theta = 0$, in HI the SNR is high even at this position where it also reaches its maximum values. Since the HI signal results from the combination of the PB and AB techniques, even if the contribution to the signal arising from AB decreases, the contribution coming from the PB is still present, determining high SNR values.

5. Conclusions

We have experimentally demonstrated that propagation-based and analyzer-based phase-contrast imaging techniques can be combined, producing original features.

Images of simple polymer fibers obtained with this hybrid method have been analyzed in terms of SNR and compared with the patterns produced independently by the two distinct techniques. Hybrid images present an almost constant value of the SNR over an angular range of the order of the FWHM of the rocking curve of the crystal analyzer.

This weak dependence on the angular positioning of the analyzer reduces the constraints in terms of optical alignment and stability of the crystal, which is one of the critical issues of the AB imaging technique.

In order to fully understand the peculiar characteristics of the HI signal, studied in a preliminary way in this paper, further theoretical and experimental investigations are required. This technique may find application in several fields already advanced by hard X-ray phase-contrast imaging, producing as high SNR as PB, while bringing the advantages of the higher refraction sensitivity of the AB technique.

This work was supported by the EU grant contract HPRI-CT-1999-50008.

References

Arfelli, F., Bonvicini, V., Bravin, A., Cantatore, G., Castelli, E., Dalla Palma, L., Di Michiel, M., Fabrizioli, M., Longo, R., Menk, R.-H., Olivo, A., Pani, S., Pontoni, D., Poropat, P., Prest, M., Rashevsky, A., Ratti, M., Rigon, L., Tromba, G., Vacchi, A., Vallazza, E. & Zanconati, F. (2000). *Radiology*, **215**, 286–293.

Born, M. & Wolf, E. (1999). *Principles of Optics: Electromagnetic Theory of Propagation, Interference and Diffraction of Light.* Cambridge University Press.

Bravin, A. (2003). *J. Phys. D*, **36**, A24–A29.
Chapman, D., Thomlinson, W., Johnston, R. E., Washburn, D., Pisano, D., Gmür, N., Zhong, Z., Menk, R., Arfelli, F. & Sayers, D. (1997). *Phys. Med. Biol.* **42**, 2015–2025.
Cloetens, P. (1999). PhD thesis. Vrije Universiteit, Brussels, Belgium.
Cloetens, P., Barrett, R., Baruchel, J., Guigay, J. & Schlenker, M. (1996). *J. Phys. D*, **29**, 133–146.
Cloetens, P., Ludwig, W., Boller, E., Peyrin, F., Schlenker, M. & Baruchel, J. (2002). *Image Anal. Stereol.* **21**, S75–S85.
David, C., Nohammer, B., Solak, H. & Ziegler, E. (2002). *Appl. Phys. Lett.* **81**, 3287–3289.
Davis, T., Gureyev, T., Gao, D., Stevenson, A. & Wilkins, S. (1995). *Phys. Rev. Lett.* **74**, 3173–3176.
Evans, A. L. (1981). *The Evaluation of Medical Images*. Bristol: Adam Hilger.
Fitzgerald, R. (2000). *Phys. Today*, **53**, 23.
Förster, E., Goetz, K. & Zaumseil, P. (1980). *Krist. Tech.* **15**, 937–945.
Hignette, O., Cloetens, P., Lee, W., Ludwig, W. & Rostaing, G. (2003). *J. Phys. IV*, **104**, 231–234.
Ingal, V. N. & Beliaevskaya, E. A. (1995). *J. Phys. D*, **28**, 2314–2317.
Lagomarsino, S., Cedola, A., Cloetens, P., Di Fonzo, S., Jark, W., Soullié, G. & Riekel, C. (1997). *Appl. Phys. Lett.* **71**, 2557–2559.
Momose, A., Takeda, T., Itai, Y. & Hirano, K. (1996). *Nature Med.* **2**, 473–475.
Nugent, K. A., Gureyev, T. E., Cookson, D. F., Paganin, D. & Barnea, Z. (1996). *Phys. Rev. Lett.* **77**, 2961–2964.
Pavlov, K. M., Gureyev, T. E., Paganin, D., Nesterets, Y. I., Morgan, M. J. & Lewis, R. A. (2004). *J. Phys. D*, **37**, 2746–2750.
Pogany, A., Gao, D. & Wilkins, S. W. (1997). *Rev. Sci. Instrum.* **68**, 2774–2782.
Snigirev, A., Snigireva, I., Kohn, V., Kuznetsov, S. & Schelokov, I. (1995). *Rev. Sci. Instrum.* **66**, 5486–5492.
Somenkov, V. A., Tkalich, A. K. & Shilstein, S. S. (1991). *Sov. Phys. Tech. Phys.* **36**, 1309–1311.
Tsai, W., Hsu, P., Hwu, Y., Chen, C., Chang, L., Je, J., Lin, H., Groso, A. & Margaritondo, G. (2002). *Nature (London)*, **417**, 139.
Wilkins, S., Gureyev, T., Gao, D., Pogani, A. & Stevenson, A. (1996). *Nature (London)*, **384**, 335–338.